ADVANCED FUNCTIONAL MATERIALS
www.afm-journal.de



# Sn-Based Nanoparticles Encapsulated in a Porous 3D Graphene Network: Advanced Anodes for High-Rate and Long Life Li-Ion Batteries

*Chao Wu, Joachim Maier, and Yan Yu**

**Sn-based materials have triggered significant research efforts as anodes for lithium-storage because of their high theoretical capacity. However, the practical applications of Sn-based materials are hindered by low capacity release and poor cycle life, which are mainly caused by structural pulverization and large volume changes on cycling. Herein, a surfactant-assisted assembly method is developed to fabricate 3D nanoarchitectures in which Sn-based nanoparticles are encapsulated by a porous graphene network. More precisely, the graphene forms a 3D cellular network, the interstices of which only partially filled by the electroactive masses, thus establishing a high concentration of interconnected nanosized pores. While the graphene-network itself guarantees fast electron transfer, it is the characteristic presence of nanosized pores in our network that leads to the favorable rate capability and cycling stability by i) accommodating the large volume expansion of Sn-based nanoparticles to ensure integrity of the 3D framework upon cycling and ii) enabling rapid access of Li-ions into Sn-based nanoparticles, which are in addition prevented from agglomerating. As a result, the 3D Sn-based nanoarchitectures deliver excellent electrochemical properties including high rate capability and stable cycle performance. Importantly, this strategy provides a new pathway for the rational engineering of anode materials with large volume changes to achieve improved electrochemical performances.**

## 1. Introduction

The development of new-generation Li-ion batteries (LIBs) with high energy density and long cycle life is of great importance for critical demands,[1–3] such as portable electronics, green electrical vehicles, and power grid. For LIB anodes, commercial graphite is far from satisfying the requirements for high energy density because of its limited theoretic capacity (372 mAh $g^{-1}$).[4] Therefore, significant research efforts[5,6] have been devoted to developing advanced anode materials with high capacity, superior cycle stability, and high rate capability. In this respect, Sn-based materials (metal,[7,8] oxides,[5] and alloy[9] have been extensively investigated as candidates for LIB anodes, as they show a high theoretical capacity and well-suited discharge potential.

One of the challenges associated with high capacity Sn-based materials is to improve capacity retention on cycling. It is known that high capacity Sn-based materials undergo large volume changes during lithiation/delithiation,[8,10] leading to pulverization of electrodes[11] and uncontrolled formation of solid electrolyte interface (SEI).[12] As a consequence, Sn-based particles lose electrical contact with each other and the current collector, resulting in a rapid capacity loss during cycling. In order to reduce the strain of Sn-based materials induced by Li insertion and extraction, several strategies have been proposed. One approach is to combine active and inactive buffering components (Co–Sn and Ni–Sn alloys).[13–15] However, they show a very limited stability enhancement because of the limited buffering effect. As an alternative approach, the size reduction of the Sn-based materials to the nanometer range has been carried out. For example, Sn-based nanoparticles,[16] hollow nanospheres,[17] nanoflakes,[18] nanotubes,[19] and nanowires[20] were reported to exhibit better mechanical stability and improved cycle performance compared to coarse grained materials. Although the nanostructure design has been successful in enhancing cyclability, it introduces a couple of new severe problems, such as poor overall electrical conduction caused by interparticle resistance and increased side reactions with electrolytes induced by high surface area.

To overcome these challenging problems, the combination of carbon and Sn-based nanomaterials has been investigated in recent years. For example, carbon-supported Sn-based nanoparticles show better cycling and an enhanced rate capability compared to pure Sn-based nanoparticles.[13,21–24] However, during the long cycling process, nanoparticles are prone to aggregate with a thick SEI layer on their surface, leading to separation between particles and carbon layer, thus decreasing the cycle life of the electrodes. Carbon-wrapped Sn-based nanoparticles have been reported to improve the cycle

Dr. C. Wu, Prof. J. Maier, Prof. Y. Yu
Max Planck Institute for Solid State Research
Heisenbergstr. 1, Stuttgart 70569, Germany
E-mail: yanyumse@ustc.edu.cn
Prof. Y. Yu
Key Laboratory of Materials for Energy Conversion
Chinese Academy of Sciences
Department of Materials Science and
Engineering University of Science and Technology of China
No. 96, Jin Zhai Rd., Hefei, Anhui 230026, China

DOI: 10.1002/adfm.201500514

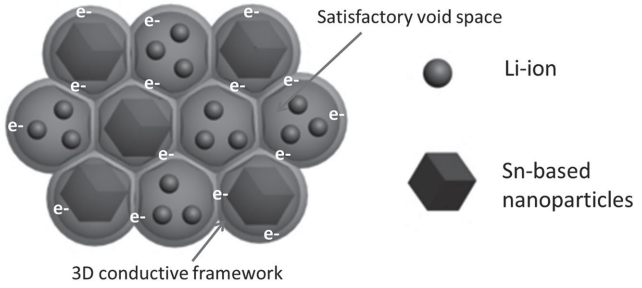


**Figure 1.** Schematic of 3D porous graphene network encapsulating Sn-based nanoparticles, showing that the internal well-defined void space can accommodate the large volume change of Sn-based particles to ensure the integrity of the overall 3D framework, and the SEI films on their surface can be stabilized on cycling.

stability.[25–28] Nonetheless, the large volume changes of Sn-based materials can damage the structure of carbon skeletons and even the battery configuration, such that the improvement in terms of cycle performance is very limited. Definitely, maintaining structure stability is a key for Sn-based anodes to achieve high electrochemical performance. Nonetheless, the rational design and fabrication of Sn-based anodes with a stabilized structure upon cycling remain a challenge.

Here, we present 3D porous graphene network-encapsulated Sn-based nanoarchitectures (0D-$CoSnO_3$⊂3D-pGN and 0D-Co–Sn⊂3D-pGN) as anodes for Li storage. While an encapsulation of active masses in a graphene network is not new,[27,28] it is the clue of one present contribution that not all of the interstices are filled by electroactive masses and a large portion remains vacant. This novel structure design, as shown in **Figure 1**, offers multiple advantages: (i) the nanoscale of Sn-based particles can suppress mechanical pulverization caused by lithiation and provide a short solid-state diffusion length for lithium; (ii) preexisting interconnected nanosized pores provide the necessary void space for expansion of Sn-based particles, preventing them from destroying the 3D framework on cycling, and allowing for fast transport of Li-ions via electrolyte filling into the percolating free interstices; and (iii) the microsized 3D conductive graphene framework can counteract self-aggregation of nanoparticles, facilitate electron transfer, and stabilize SEI formation. As a consequence, the $CoSnO_3$⊂pGN and Co–Sn⊂pGN nanoarchitectures exhibit high reversible capacity and fast rate capability, as well as ultralong cycle life.

## 2. Result and Discussion

### 2.1. Synthesis and Characterization

The bottom-up assembly provides an attractive path for synthesizing unique nanostructures because of low-cost and simplicity of fabrication.[29] In nature, the assembly route creates many complex composite systems with synergetic functions unavailable for the individual components.[30] The surfactant-assisted bottom-up assembly approach to fabricate the 3D porous graphene Sn-containing network involves two main steps, as shown in **Figure 2**a. First, the building blocks consisting of graphene oxide (GO), polystyrene (PS) latex particles, and the $CoSn(OH)_6$ nanoparticles were uniformly dispersed into aqueous solution. After dropwise adding the cationic surfactant (cetyltrimethyl ammonium bromide, CTAB) solution, these building blocks assembled into aggregate, leaving clearly transparent solution. GO possesses large amounts of oxygen-containing groups on its skeleton, rendering its surface negatively charged in aqueous solution.[31] Thus, GO can capture cationic CTAB molecules, leading to a hydrophilic-to-hydrophobic transformation of the GO surface. This hydrophobic interaction between GO sheets provides the driving force of assembly. After reduction of GO, the coagulum was further annealed under different atmospheres to obtain the desired $CoSnO_3$⊂pGN and Co–Sn⊂pGN, respectively. Note that the assembly process is conducted in aqueous solution and the building blocks do not need any presurface treatment, making this fabrication route environment friendly and facile.

Graphene, the 2D single-layer graphite sheet, exhibits many unique and amazing properties such as high electrical conductivity, high surface area, and excellent chemical stability.[32–34] These properties make graphene a good carbon candidate to improve the electrochemical properties of Sn-based materials. So far, many approaches have been proposed to prepare graphene, including chemical vapor deposition (CVD) growth, organic synthesis, direct exfoliation of graphite, and reduction of graphite derivatives.[35] Compared to other methods, reduction of GO is low-cost and scalable.[36] In this study, we select soluble GO as precursor to fabricate $CoSnO_3$⊂pGN. Cube-like $CoSn(OH)_6$ nanoparticles were utilized as precursor to prepare $CoSnO_3$. $CoSn(OH)_6$ nanoparticles were synthesized by a sol–gel method. As shown in Figure 2b, X-ray diffraction (XRD) analysis of the produced sample demonstrates that all diffraction peaks are indexed to crystalline $CoSn(OH)_6$ (JCPD card no. 13-356). After annealing at 400 °C in Ar atmosphere, the XRD pattern of the obtained $CoSnO_3$ nanoparticles show a broad diffraction peak, suggesting the nanoparticles to be amorphous solids. Figure 2c presents a scanning electron microscopy (SEM) image of $CoSnO_3$ nanoparticles. Cube-like nanoparticles were observed in a size range from about 50 to 100 nm. Transmission electron microscopy (TEM) further reveals that the single $CoSnO_3$ particle is porous, probably because of the removal of water molecules.[37,38] Moreover, 3D graphene network-encapsulated $CoSnO_3$ ($CoSnO_3$⊂GN) composites were fabricated by the same process as $CoSnO_3$⊂pGN. Figure 2d shows a typical SEM image of $CoSnO_3$⊂GN. Most of the $CoSnO_3$ nanoparticles are encapsulated by graphene sheets connected into a microsized 3D network. The microstructure and morphology of $CoSnO_3$⊂pGN were investigated by XRD and SEM, too. The diffraction pattern of $CoSnO_3$⊂pGN is similar to that of the $CoSnO_3$ nanoparticles, indicating that the encapsulated $CoSnO_3$ nanoparticles are also amorphous solids. Compared to $CoSnO_3$⊂GN, polystyrene nanospheres were utilized as sacrificial template to create void space for $CoSnO_3$⊂pGN during the fabrication process. Thus, microsized $CoSnO_3$⊂pGN shows a large amount of nanosized pores which surround the $CoSnO_3$ particles and enable to accommodation of the volume explanation of $CoSnO_3$ particles (Figure 2e,f and Figure S1, Supporting Information). The diameters of the produced pores range from about 100 to 200 nm which is comparable to the size of $CoSnO_3$ particles. In addition, the volume of nanosized pores can be tuned by the

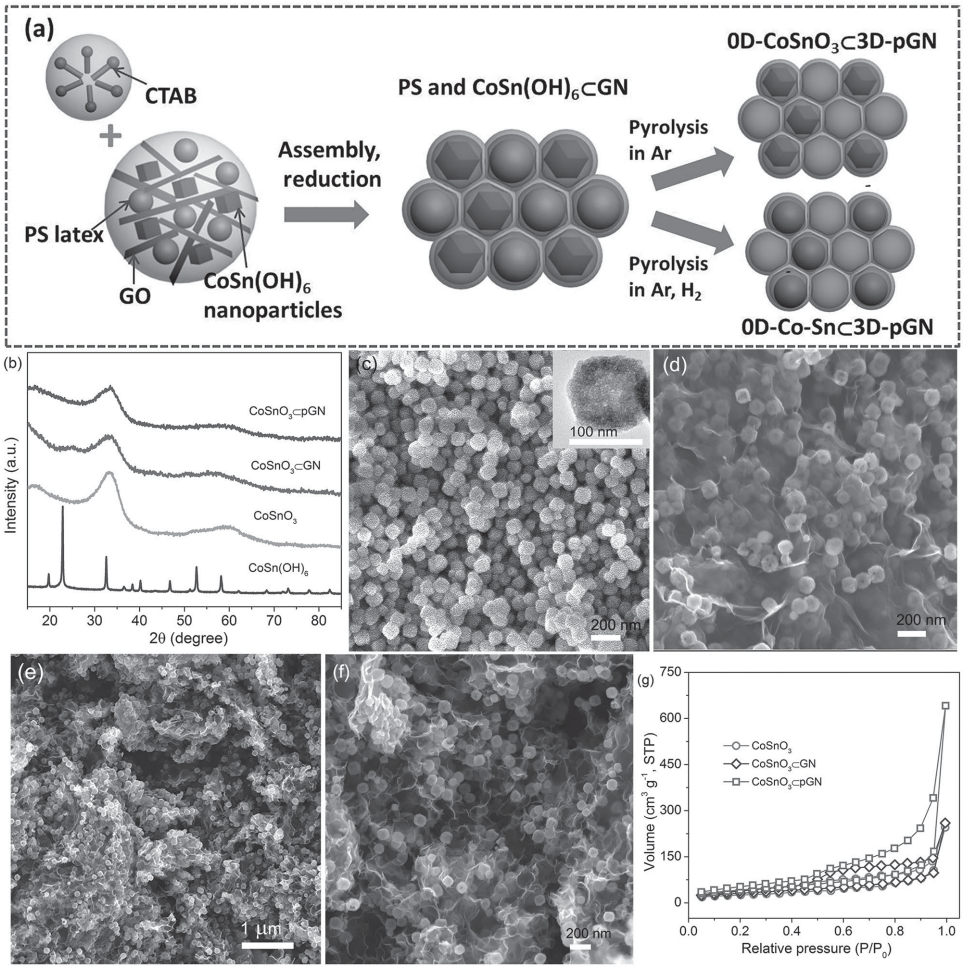


**Figure 2.** a) Fabrication of 3D porous graphene network-encapsualted Sn-based nanocomposites ($CoSnO_3$⊂pGN and Co–Sn⊂pGN). b) XRD patterns of the $CoSn(OH)_6$ precursor, $CoSnO_3$ nanoparticles, $CoSnO_3$⊂GN, and $CoSnO_3$⊂pGN. c) SEM image of $CoSnO_3$ nanoparticles, and inset showing TEM image of a single nanoparticle. d) SEM image of $CoSnO_3$⊂GN, showing that most of $CoSnO_3$ nanoparticles are encapsulated by graphene network. e) SEM image and f) magnified SEM image of $CoSnO_3$ ⊂pGN, showing that most of $CoSnO_3$ nanoparticles are embeded in the porous graphene network. g) $N_2$ adsorption/desorption isotherms of $CoSnO_3$ nanoparticles, $CoSnO_3$⊂GN, and $CoSnO_3$⊂pGN.

mass ratio of polystyrene nanospheres and $CoSn(OH)_6$ nanoparticles. To ensure the integrity of the graphene network, a sufficient internal void space is required for the $CoSnO_3$ expansion during the lithiation process. Taking into account that the density of $CoSnO_3$ is much higher than that of polystyrene, we chose a mass ratio of (1:1) for polystyrene to $CoSnO_3$. Polystyrene nanospheres serve as sacrificial templates to provide a void space for $CoSnO_3$⊂pGN, which is further confirmed by the Brunauer–Emmett–Teller adsorption measurements (Figure 2g). $CoSnO_3$ nanoparticles show a specific surface area of 90 $m^2\ g^{-1}$ and a total pore volume of 0.38 $cm^3\ g^{-1}$, which is close to those of $CoSnO_3$⊂GN (112.8 $m^2\ g^{-1}$ and 0.4 $cm^3\ g^{-1}$). Such results indicate that the pore volume for $CoSnO_3$⊂GN originates from the $CoSnO_3$ nanoparticles because of their porous nanostructure. For $CoSnO_3$⊂pGN, the specific surface area and total pore volume reach 150.4 $m^2\ g^{-1}$ and 0.99 $cm^3\ g^{-1}$, respectively, much higher than values for $CoSnO_3$⊂GN.

To further demonstrate the important role of the pores in our graphene network for improving the electrochemical properties of Sn-based materials, Co–Sn⊂pGN and Co–Sn⊂GN were synthesized under a reducing atmosphere (argon with 5% hydrogen). **Figure 3**a displays XRD patterns of the produced samples. The Co–Sn alloy of the resulting samples is composed of CoSn (JCPD card no. 002-0559) and $Co_3Sn_2$ (JCPD card no. 027-1124). SEM images of Co–Sn⊂GN show that the Co–Sn particles are encapsulated by the 3D graphene cellular network. In spite of graphene wrapping, the Co–Sn alloy particles are observed with a size between 30 and 70 nm. Notably, no void space around Co–Sn alloy particles is detected in SEM (Figure 3b,c). For Co–Sn⊂pGN, however, large amounts of nanosized pores are observed into the graphene networks and provide void space for buffering the volume expansion of the Co–Sn alloy (Figure 3d-f).

### 2.2. Electrochemical Performances

The electrochemical performance of the prepared Sn-based materials is evaluated by coin-type cells with Li metal as counter electrode. **Figure 4**a shows the cyclic voltammetry (CV)

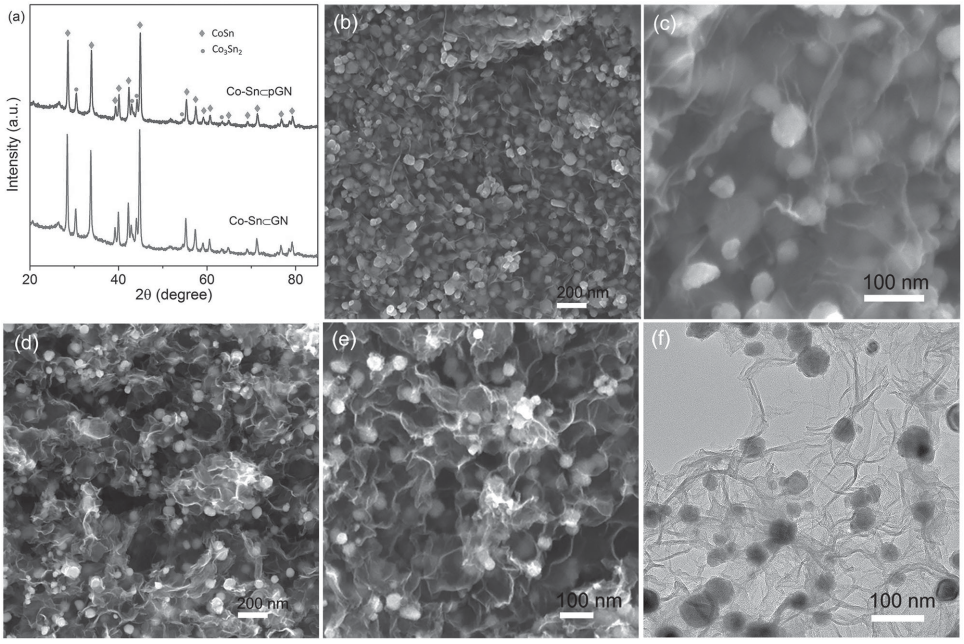


**Figure 3.** a) XRD patterns of Co–Sn⊂GN and Co–Sn⊂pGN. b,c) SEM images of Co–Sn⊂GN. d,e) SEM and f) TEM images of Co–Sn⊂pGN, showing that the void space is distributed around the Co–Sn alloy nanoparticles.

curve of a $CoSnO_3 \subset$ pGN electrode in the range from 0.001 to 3 V, recorded at a scan rate of 0.1 mV $s^{-1}$. In the first discharge cycle, several cathodic peaks are observed. The peak at 1.4 V is ascribed to the reduction of $CoSnO_3$ into CoO, metallic Sn, and $Li_2O$.[39] The peaks at around 0.7 and 0.1 V correspond to the further reduction of CoO into metallic Co[40] and lithium alloying of Sn, respectively. The detailed conversion reaction mechanism is as follows:[39]

$$CoSnO_3 + 4Li^+ + 4e^- \rightarrow CoO + Sn + 2Li_2O \quad (1)$$

$$CoO + 2Li^+ + 2e^- \rightarrow Co + Li_2O \quad (2)$$

$$Sn + \chi Li + \chi e^- \leftrightarrow Li_\chi Sn \quad (3)$$

In the charge process, the peaks located at around 0.5 and 1.1 V and 2.0 V are ascribed to extraction of lithium from the discharge products.

Figure 4b shows representative galvanostatic charge/discharge profiles of a $CoSnO_3$⊂pGN electrode at a current density of 1 A $g^{-1}$ within a cut-off voltage window between 0.005 and 3 V. The initial discharge and charge capacities are 1380 and 873 mAh $g^{-1}$, respectively, corresponding to a Coulombic efficiency (CE) of 63%. In this study, all the specific capacities are calculated on basis of the total mass of graphene and $CoSnO_3$. The capacity loss may be caused by the formation of SEI films and electrolyte decomposition. In addition, the $CoSnO_3$ and $CoSnO_3$⊂GN electrodes show similar charge/discharge profiles as $CoSnO_3$⊂pGN (Figure 4b). $CoSnO_3$⊂GN delivers an initial discharge capacity of 1296 mAh $g^{-1}$ and a CE of 69% while $CoSnO_3$ nanoparticles display a discharge capacity of 1480 mAh $g^{-1}$ and a CE of only 40% at the same current density. Compared to $CoSnO_3$ nanoparticles, the higher CE values of $CoSnO_3$⊂pGN and $CoSnO_3$⊂GN should be attributed to the presence of the graphene network encapsulation. Graphene network not only reduces the SEI formation by avoiding the direct contact between $CoSnO_3$ nanoparticles and electrolyte but also improve the electronic conductivity of $CoSnO_3$ nanoparticles to facilitate the lithium extraction. Note that the capacities of $CoSnO_3$⊂pGN and $CoSnO_3$⊂GN calculated based on the mass of composites. So the $CoSnO_3$⊂pGN and $CoSnO_3$⊂GN electrodes show shorter discharge plateaus around 1.4 V when compared to the $CoSnO_3$ electrode because graphene has no discharge plateau at 1.4 V.[41] Figure S2 (Supporting Information) shows the charge/discharge profiles of the $CoSnO_3$⊂pGN and $CoSnO_3$⊂GN electrodes, and their capacities are calculated based on the mass of $CoSnO_3$. The lengths of the plateau around 1.4 V for the $CoSnO_3$⊂pGN and $CoSnO_3$⊂GN electrodes are close to that for the $CoSnO_3$ electrode. Similar phenomenon was reported in the previous study of graphene–metal oxide composites.[27,41]

Cycling stability of Sn-based materials is naturally a most important parameter for the applicability. The cycle performance for the three types of materials is given in Figure 4c. The simple $CoSnO_3$ electrode undergoes a rapid capacity decay. After 200 cycles, only a capacity of 30 mAh $g^{-1}$ is available. Such poor cycle stability is consistent with the result of previously reported Sn-based materials[42,43] because of large volume expansion and the continuous formation of SEI film. For $CoSnO_3$⊂GN, the capacity is stable for the initial 25 cycles but afterwards drops rapidly with a residual capacity of 278 mAh $g^{-1}$ after 200 cycles. The initial cycle stability is ascribed to the 3D graphene network encapsulation. With battery cycling, graphene networks are gradually destroyed by the huge volume change of internal $CoSnO_3$ particles, leading to

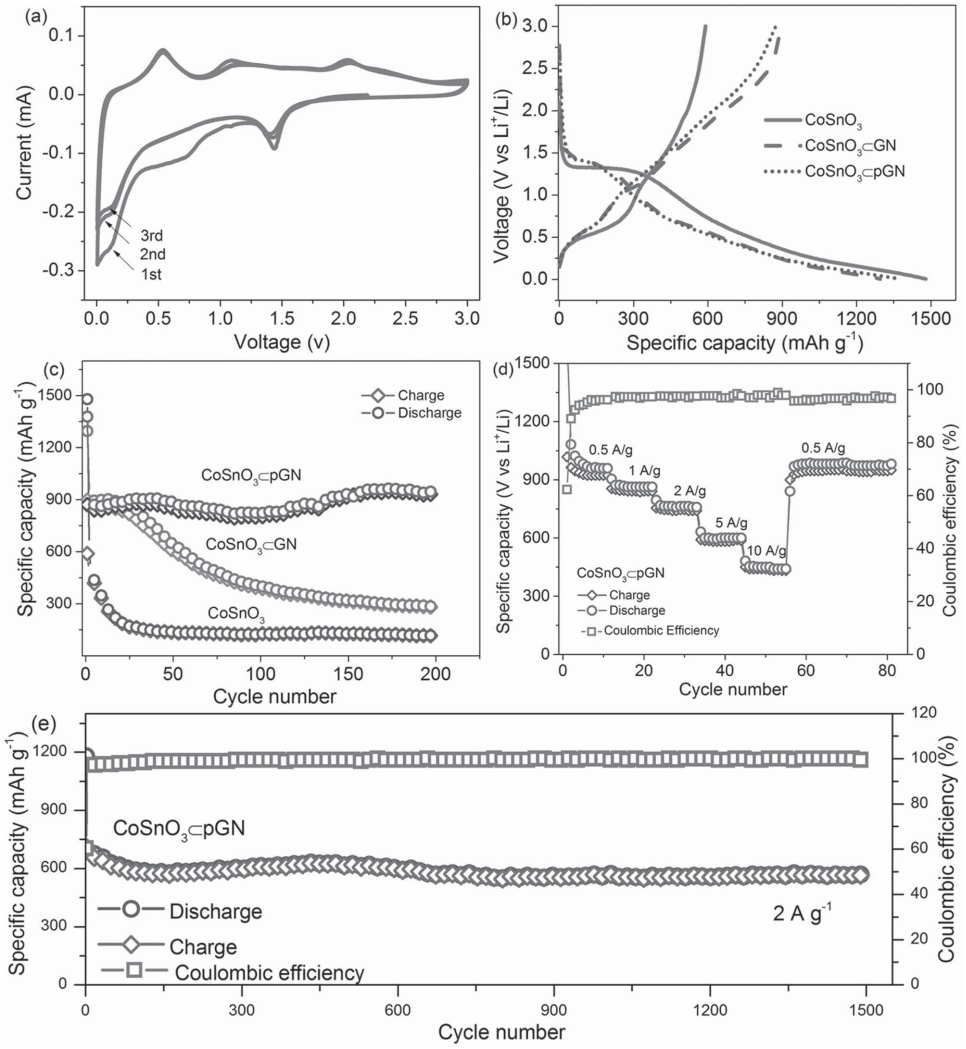


**Figure 4.** a) CV profiles of the $CoSnO_3$⊂pGN electrode recorded at a scan of 0.1 mV $s^{-1}$. b) The first charge/discharge voltage profiles and c) cycle performance of the $CoSnO_3$, $CoSnO_3$⊂GN, and $CoSnO_3$ ⊂ pGN electrodes at the current density of 1 A $g^{-1}$. d) Rate capability of the $CoSnO_3$⊂pGN electrode at various current density (from 0.5 to 10 A $g^{-1}$). e) Cycle performance of the $CoSnO_3$⊂pGN electrode at the current density of 2 A $g^{-1}$.

fast capacity fading. Remarkably, the $CoSnO_3$⊂pGN electrode shows a very stable cyclability. After 200 cycles, it still delivers a reversible capacity of 925 mAh $g^{-1}$ without any fading, which is much higher that of the $CoSnO_3$ nanoparticles and $CoSnO_3$⊂GN. Moreover, the cycle stability is much better than that of previously reported $CoSnO_3$ nanoparticles,[44] carbon-coated $CoSnO_3$ nanocomposites,[45] graphene-wrapped $CoSnO_3$ nanocomposites.[46] Compare to the $CoSnO_3$ and $CoSnO_3$⊂GN electrodes, polystyrene nanospheres were utilized as sacrificial template to make enough internal void space for the $CoSnO_3$ ⊂ pGN electrode. These internal void spaces can buffer the volume expansion of active particles and preserve graphene networks to assure the electrode structure integrity on cycling. On the other side, graphene skeletons stabilize the formation of SEI films. Figure S3 (Supporting Information) shows the SEM images of $CoSnO_3$ nanoparticle, $CoSnO_3$⊂GN, and $CoSnO_3$⊂pGN electrodes after 200 cycles. One can see that the $CoSnO_3$ nanoparticles and $CoSnO_3$⊂GN are wrapped by thick SEI films, and it is difficult to make out the cube-like morphology of $CoSnO_3$ nanoparticles. In contrast, the morphology of $CoSnO_3$ and void space are still preserved after cycling for the $CoSnO_3$⊂pGN electrode because of the protection of porous graphene networks. As discussed previously, the 3D porous graphene network plays a decisive role for cycle stability. In order to make a complete 3D graphene network, enough graphene content is required for the $CoSnO_3$⊂pGN composite. Previous study indicates that 10 wt% graphene can construct a complete conductive network that penetrates the graphene/polystyrene composite.[31] Therefore, in this study, the graphene content of the PS and $CoSn(OH)_6$⊂GN precursor reaches 10 wt% to ensure that graphene can form a 3D network in the gaps between PS nanospheres and $CoSn(OH)_6$ nanoparticles. After annealing at 400 °C in argon, the PS template was removed and the 3D porous graphene network (25 wt%) was obtained for the $CoSnO_3$⊂pGN composites.

$CoSnO_3$⊂pGN was further investigated by galvanostatic charge/discharge at various current rates from 0.5 to 10 A $g^{-1}$. As shown in Figure 4d, after 10 cycles at a low current density of

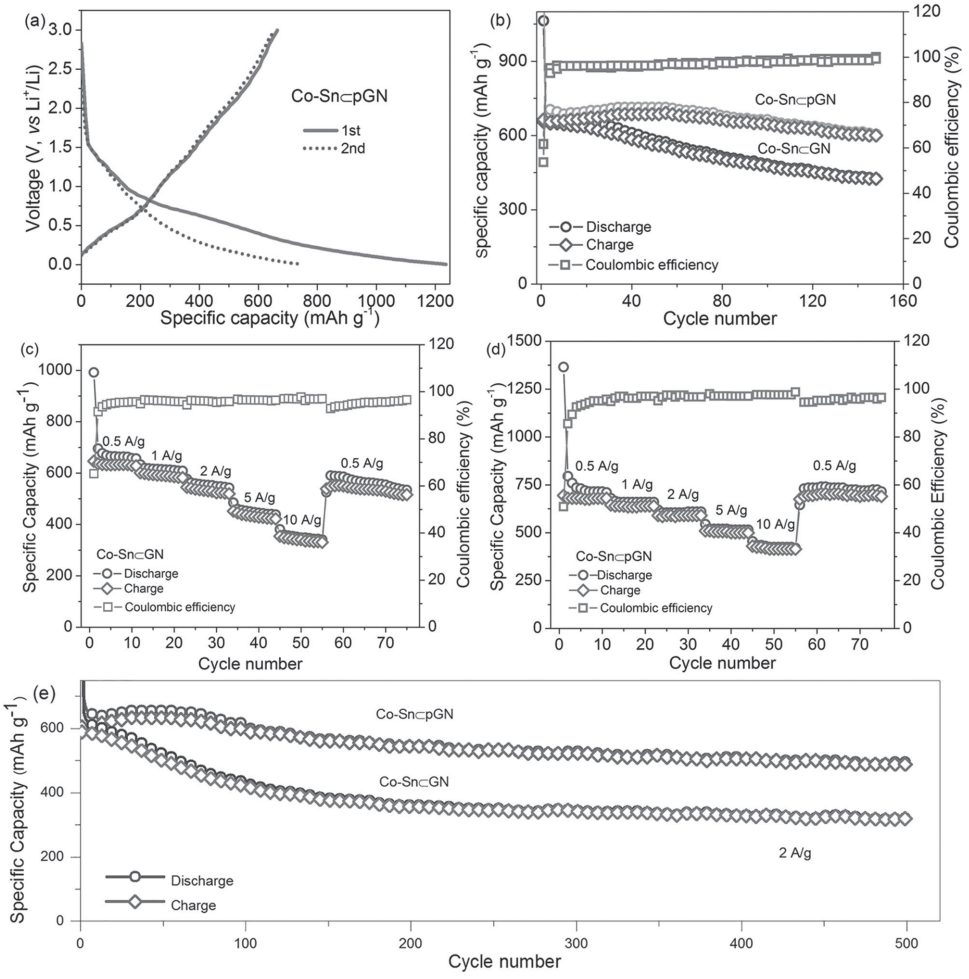


**Figure 5.** a) The initial charge–discharge profiles of Co–Sn ⊂ pGN. b) Cycle performance of the Co–Sn ⊂ GN and Co–Sn ⊂ pGN electrodes at the current density of 1 A $g^{-1}$. Rate capability of the c) Co–Sn ⊂ GN and d) Co–Sn ⊂ pGN electrodes at different current density (from 0.5 to 10 A $g^{-1}$). Cycle tests of the e) Co–Sn ⊂ GN and d) Co–Sn ⊂ pGN electrodes at the current density of 2 A $g^{-1}$.

0.5 A $g^{-1}$, the $CoSnO_3$⊂pGN electrode shows a reversible capacity of 923 mAh $g^{-1}$. As the current density increases to 1 A $g^{-1}$, a specific capacity of 841 mA $g^{-1}$ is available and afterwards the capacity gradually decreases to 741 mAh $g^{-1}$ at 2 A $g^{-1}$ and 586 mAh $g^{-1}$ at 5 A $g^{-1}$. Notably, even at a high current density of 10 A $g^{-1}$, the reversible capacity reaches 432 mAh $g^{-1}$, which is still higher than theoretical capacity of commercial graphite. Such value is also higher than that of the $CoSnO_3$ and the $CoSnO_3$⊂GN electrodes and of other Sn-based materials.[23,47,48] As shown in Figure S4 (Supporting Information), they deliver a reversible capacity of 25 and 249 mAh $g^{-1}$ after 55 cycles at the current density of 10 A $g^{-1}$. The remarkable rate capability of $CoSnO_3$⊂pGN should benefit from 3D conductive framework that facilitates electron transfer and from the porous nanostructure that allows for the rapid access of Li-ions into the particle bulk. Importantly, the specific capacity of $CoSnO_3$⊂pGN electrode nearly recovers to the original value when the current density returns to 0.5 A $g^{-1}$ after high-rate cycling, demonstrating that porous graphene networks can maintain the structure integrity of electrodes. To further verify the excellent cycle stability, we cycled the $CoSnO_3$⊂pGN battery for 1500 cycles at the current density of 2 A $g^{-1}$ (Figure 4e). After 1500 cycles, the $CoSnO_3$⊂pGN electrodes show a reversible capacity of 566 mAh $g^{-1}$, corresponding to retention of 80% (0.013% loss for per cycle). Such value is higher than that of the reported Sn-based materials.[49,50]

**Figure 5**a shows the charge/discharge voltage profiles of Co–Sn⊂pGN for the first and second cycles at a current density of 1 A $g^{-1}$ within 0.005–3 V. The initial discharge and charge capacities of Co–Sn⊂pGN reach 1236 and 664 mAh $g^{-1}$, respectively, corresponding to a CE of 54%. In the second cycle, it delivers a reversible capacity of 655 mAh $g^{-1}$ and the corresponding CE increases to 87%. The initial low CE is mainly ascribed to the formation of SEI films and electrolyte decomposition. Notably, the Co–Sn ⊂ pGN electrode also displays a remarkable cycling performance. As shown in Figure 5b, after 150 cycles, a reversible capacity of 595 mAh $g^{-1}$ is available, corresponding to retention of 90%. For comparison, Co–Sn⊂GN delivers a reversible capacity of only 422 mAh $g^{-1}$ after 150 cycles, and the corresponding retention is only 64%, demonstrating the robustness of 3D porous graphene networks. The rate performance of Co–Sn⊂GN and Co–Sn⊂pGN is

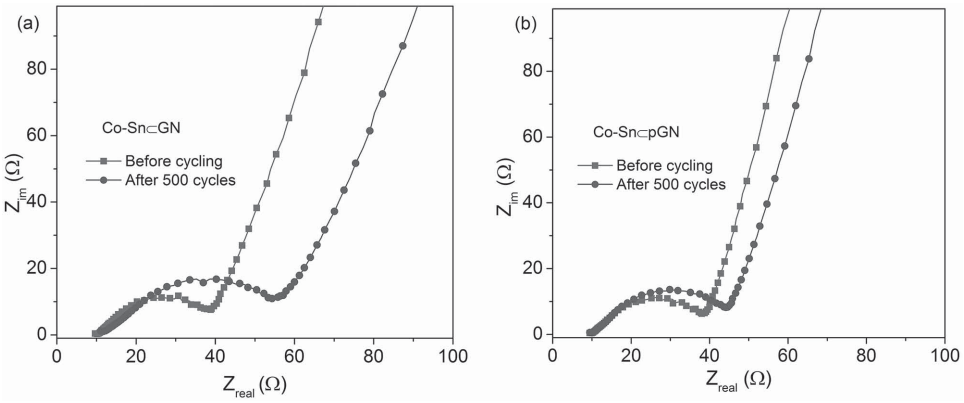


**Figure 6.** Electrochemical impedance spectra of the a) Co–Sn ⊂ GN and b) Co–Sn ⊂ pGN electrodes before and after 500 cylces.

shown in Figure 5c,d. The initial reversible capacities of Co–Sn ⊂GN and Co–Sn⊂pGN are as high as 646 and 695 mAh $g^{-1}$, respectively, at a current density of 0.5 A $g^{-1}$. However, as the current density increases, the capacity gap between Co–Sn⊂GN and Co–Sn⊂pGN is also increased, indicating that porous graphene network is beneficial for improving rate capability. At the high current density of 10 A $g^{-1}$, Co–Sn⊂pGN delivers a high capacity of 430 mAh $g^{-1}$ as a result of the unique nanostructure, which is higher than that for previously reported Sn-based alloys.[13,22,25] For Co–Sn⊂GN, only a reversible capacity of 349 mAh $g^{-1}$ at 10 A $g^{-1}$ is available because it is difficult for electrolyte to penetrate into micrometer-sized Co–Sn ⊂ GN agglomeration. Figure 5e exhibits the long cycling performance of Co–Sn⊂pGN and Co–Sn⊂GN electrodes. After 500 cycles, the reversible capacity of Co–Sn⊂pGN reaches 489 mAh $g^{-1}$, corresponding to retention of 81% at the current density of 2 A $g^{-1}$. In contrast, the capacity of Co–Sn⊂GN drops rapidly afterward with a remaining capacity of only 319 mAh $g^{-1}$ after 500 cycles, corresponding to retention of 54%. Such results also suggest that 3D porous frameworks can accommodate large volume change of Co–Sn alloy and remain the electrode structure stable. Compared to the $CoSnO_3$⊂pGN electrode, the Co–Sn⊂pGN electrode shows inferior electrochemical performance in terms of reversible capacity, rate capability, and cycle stability, which is attributed to high theoretic capacity and porous nanostructure for the $CoSnO_3$ particles. Porous nanostructure provides rapid ion diffusion channels and mitigates the strain effect caused by volume change on cycling. For the Co–Sn alloy particles, no porous structure is found because of undergoing a high temperature reduction process (800 °C, Ar/$H_2$ atmosphere). However, similar to the $CoSnO_3$⊂pGN electrode, the Co–Sn⊂pGN electrode shows better electrochemical performance than the Co–Sn⊂GN electrode due to the presence of porous 3D graphene framework.

In order to further understand the remarkable cycling performance of the Co–Sn⊂pGN electrode, the electrochemical impedance spectra of the Co–Sn⊂GN and Co–Sn⊂pGN electrodes were analyzed before cycling and after 500 cycles. As shown in **Figure 6**, all Nyquist plots show a depressed semicircle in the medium frequency region, which is associated with internal resistances in the electrode.[24] Before cycling, the effective resistance of the Co–Sn⊂pGN electrode is close to that of the Co–Sn⊂GN electrode. After 500 cycles, the resistance increase for the Co–Sn⊂pGN electrode is significantly lower than that for the Co–Sn⊂GN electrode, implying that the electrode structure of the Co–Sn⊂GN is very stable during the long cycling process. This result further confirms that 3D porous graphene network is not damaged during cycling.

## 3. Conclusion

In summary, we develop a surfactant-assisted assembly method for rational design and fabrication of 3D porous graphene network-encapsulated Sn-based architectures. The graphene frameworks are able to improve the overall electrical conductivity of the electrodes and to stabilize the SEI formation. The interstices of the cellular framework are only partially filled, thus providing a high concentration of interconnected nanosized pores. It is the presence of pores in the nanostructure that facilitates the access of Li-ions into Sn-based nanoparticles, and also accommodates the large volume expansion of Sn-based nanoparticles, preserving the integrity of the 3D graphene-network during the long cycling process. Such produced $CoSnO_3$⊂pGN and Co–Sn⊂pGN show excellent electrochemical performances, including long cycle life and high rate capabilities. This 3D porous encapsulation design principle provides a novel pathway for high capacity anode materials with large volume changes to improve the electrochemical properties. In addition, the surfactant-assisted assembly process is conducted in the aqueous solution without any modification for building blocks, indicating that it is a facile, environment-friendly, and scalable technique. We believe that this fabrication method is also of use for other graphene-based functional materials.

## 4. Experimental Section

*Synthesis of $CoSnO_3$ Nanoparticles*: First, 1 mmol $Co(NO_3)_2{\cdot}6H_2O$ and 1 mmol $SnCl_4{\cdot}5H_2O$ were dissolved into 15 mL deionized water. The two solutions were mixed by magnetic stirring, and then added by 1 mmol sodium citrate. Subsequently, the resulted solution was added stepwise by 5 mL NaOH (2 M) solution. After stirring for 1 h, the $CoSn(OH)_6$ nanoparticles are available by centrifugation separation and washing by deionized water. The desired $CoSnO_3$ nanoparticles were obtained by annealing the $CoSn(OH)_6$ precursor in argon at 400 °C for 2 h.

*Fabrication of $CoSnO_3$⊂pGN and $CoSnO_3$⊂GN*: In a typical process, GO (100 mg) was first dispersed into 30 mL aqueous solution. GO was synthesized by modified Hummers' method.[31] Then, 20 mL $CoSn(OH)_6$ (0.19 g) aqueous dispersion and 20 mL polystyrene (0.15 g) emulsion were dispersed into the GO solution. Polystyrene emulsion nanoparticles were synthesized according to previous study.[31] Next, 10 mg CTAB was dissolved in 10 mL deionized water. The CTAB solution was added stepwise into the above mixture under the stirring condition to form coagulum. The resulted coagulum was separated by vacuum filtration and then reduced by hydrazine. The resulted product was annealed in argon at 400 °C for 2 h to obtain the desired $CoSnO_3$⊂pGN. The preparation process of $CoSnO_3$⊂GN is similar with $CoSnO_3$⊂pGN but do not include polystyrene emulsion. The content of graphene for the composites is about 25 wt% by the following equation: $W = (1 - M_1/M_2)\times 100\%$, where $W$ is the graphene content of the composites; $M_1$ and $M_2$ are the mass of the composites before and after annealing at 650 °C in air, respectively. Graphene is decomposed into gas beyond 400 °C in air, but $CoSnO_3$ is stable at 650 °C in air.[27]

*Fabrication of Synthesis of Co–Sn⊂pGN and Co–Sn⊂GN*: In a typical process, GO (100 mg) was first dispersed into 30 mL aqueous solution. Then, 20 mL $CoSn(OH)_6$ (0.19 g) aqueous dispersion and 20 mL polystyrene (0.15 g) emulsion were dispersed into the GO solution. Next, 10 mg CTAB was dissolved in 10 mL deionized water. The CTAB solution was added stepwise into the above mixture under the stirring condition to form coagulum. The resulted coagulum was separated by vacuum filtration and then reduced by hydrazine. The resulted product was annealed in argon with 5 wt% hydrogen at 800 °C for 2 h to obtain the desired Co–Sn⊂pGN. A similar process was used to fabricate Co–SnÌGN but does not include polystyrene emulsion.

*Materials Characterization*: The morphology and microstructure of the as-prepared samples were investigated by field-emission scanning electron microscopy (FE-SEM, Zeiss Gemini DSM 982) and TEM (JEM-2010, JEOL). Nitrogen adsorption and desorption isotherms were measured with a Quanta Chrome Adsorption Instrument. The structures of the as-prepared samples were recorded by XRD (Philips) using Cu Ka radiation.

*Electrochemical Measurement*: The electrochemical performance of materials was carried out by the 2032-type coin-cell with a metallic lithium film as the counter electrode. The working electrodes were made by casting slurry containing active material (graphene-Sn-based composites or $CoSnO_3$ nanoparticles), carbon black, and (polyvinylidene fluoride) PVDF binder with a mass ration of 8:1:1 on a Cu foil. The electrodes were dried at 80 °C for 12 h and then assembled into the coin cells in a glove filled with argon. The mass loading of active material is controlled around 1.5 mg $cm^{-2}$ and the film thickness is in the range of 20–30 μm. The electrolyte is composed of 1 M $LiPF_6$ in the ethylene carbonate/diethyl carbonate (1:1 v/v). The galvanostatic charge–discharge tests were performed on a battery system (Neware BTS-610) within a cutoff voltage range from 0.005 to 3 V. For the $CoSnO_3$⊂GN and $CoSnO_3$⊂pGN electrodes, the specific capacity was calculated based on the mass of graphene/$CoSnO_3$ composite. For the Co–Sn⊂GN and Co–Sn⊂pGN electrodes, the specific capacity was calculated based on the mass of graphene and Co–Sn alloy. Cyclic voltammetry measurements were carried out by an electrochemical workstation (VoltaLab 80) at a scanning rate of 0.1 mV $s^{-1}$. Electrochemical impedance spectrum measurements were performed on an electrochemical workstation (VoltaLab 80) in the frequency range from 100 KHz to 0.1 Hz.

## Supporting Information

Supporting Information is available from the Wiley Online Library or from the author.

## Acknowledgements

This work was financially supported by the Sofja Kovalevskaja award of the Alexander von Humboldt Foundation, by the National Natural Science Foundation of China (Grant Nos. 21171015 and 21373195), the Recruitment Program of Global Experts, program for New Century Excellent Talents in University (NCET), the Fundamental Research Funds for the Central Universities (WK2060140014 and WK2060140016), the Collaborative Innovation Center of Suzhou Nano Science and Technology and the Max Planck Society.

Received: February 6, 2015
Revised: March 24, 2015
Published online: May 6, 2015

[1] M. Armand, J. M. Tarascon, *Nature* **2008**, *451*, 652.
[2] I. Kovalenko, B. Zdyrko, A. Magasinski, B. Hertzberg, Z. Milicev, R. Burtovyy, I. Luzinov, G. Yushin, *Science* **2011**, *334*, 75.
[3] B. Dunn, H. Kamath, J.-M. Tarascon, *Science* **2011**, *334*, 928.
[4] J. Jiang, Y. Li, J. Liu, X. Huang, C. Yuan, X. W. Lou, *Adv. Mater.* **2012**, *24*, 5166.
[5] S. Yang, W. B. Yue, J. Zhu, Y. Ren, X. J. Yang, *Adv. Funct. Mater.* **2013**, *23*, 3570.
[6] D. Deng, M. G. Kim, J. Y. Lee, J. Cho, *Energy Environ. Sci.* **2009**, *2*, 818.
[7] Y. Yu, L. Gu, X. Y. Lang, C. B. Zhu, T. Fujita, M. W. Chen, J. Maier, *Adv. Mater.* **2011**, *23*, 2443.
[8] Z. Zhu, S. Wang, J. Du, Q. Jin, T. Zhang, F. Cheng, J. Chen, *Nano Lett.* **2014**, *14*, 153.
[9] X. L. Wang, W. Q. Han, J. J. Chen, J. Graetz, *ACS Appl. Mater. Interfaces* **2010**, *2*, 1548.
[10] J. Y. Huang, L. Zhong, C. M. Wang, J. P. Sullivan, W. Xu, L. Q. Zhang, S. X. Mao, N. S. Hudak, X. H. Liu, A. Subramanian, H. Fan, L. Qi, A. Kushima, J. Li, *Science* **2010**, *330*, 1515.
[11] B. Wang, B. Luo, X. Li, L. Zhi, *Mater. Today* **2012**, *15*, 544.
[12] H. Zhu, Z. Jia, Y. Chen, N. Weadock, J. Wan, O. Vaaland, X. Han, T. Li, L. Hu, *Nano Lett.* **2013**, *13*, 3093.
[13] J. R. Gonzalez, R. Alcantara, F. Nacimiento, J. L. Tirado, *Electrochim. Acta* **2011**, *56*, 9808.
[14] B. O. Jang, S. H. Park, W. J. Lee, *J. Alloys Compd.* **2013**, *574*, 325.
[15] H. Guo, S. Zhao, H. Zhao, Y. Chen, *Electrochim. Acta* **2009**, *54*, 4040.
[16] Q. Guo, X. Qin, *J. Solid State Electrochem.* **2014**, *18*, 1031.
[17] X. W. Lou, Y. Wang, C. Yuan, J. Y. Lee, L. A. Archer, *Adv. Mater.* **2006**, *18*, 2325.
[18] L. Zhang, G. Zhang, H. B. Wu, L. Yu, X. W. Lou, *Adv. Mater.* **2013**, *25*, 2589.
[19] C. Zhu, X. Xia, J. Liu, Z. Fan, D. Chao, H. Zhang, H. J. Fan, *Nano Energy* **2014**, *4*, 105.
[20] Y.-L. Ding, Y. Wen, P. A. van Aken, J. Maier, Y. Yu, *Nanoscale* **2014**, *6*, 11411.
[21] X. Liu, J. Cheng, W. Li, X. Zhong, Z. Yang, L. Gu, Y. Yu, *Nanoscale* **2014**, *6*, 7817.
[22] P. Chen, L. Guo, Y. Wang, *J. Power Sources* **2013**, *222*, 526.
[23] L. Xifei, A. Dhanabalan, G. Lin, W. Chunlei, *Adv. Energy Mater.* **2012**, *2*, 238.
[24] Z. Wen, S. Cui, H. Kim, S. Mao, K. Yu, G. Lu, H. Pu, O. Mao, J. Chen, *J. Mater. Chem.* **2012**, *22*, 3300.
[25] B. O. Jang, S. H. Park, W. J. Lee, *J. Alloys Compd.* **2013**, *574*, 325.
[26] B. Luo, B. Wang, M. Liang, J. Ning, X. Li, L. Zhi, *Adv. Mater.* **2012**, *24*, 1405.
[27] Y. Cao, L. Zhang, D. Tao, D. Huo, K. Su, *Electrochim. Acta* **2014**, *132*, 483.
[28] H. Yang, Z. Hou, N. Zhou, B. He, J. Cao, Y. Kuang, *Ceram. Int.* **2014**, *40*, 13903.
[29] J. Y. Cheng, A. M. Mayes, C. A. Ross, *Nat. Mater.* **2004**, *3*, 823.
[30] J. F. Banfield, S. A. Welch, H. Z. Zhang, T. T. Ebert, R. L. Penn, *Science* **2000**, *289*, 751.

[31] C. Wu, X. Huang, G. Wang, L. Lv, G. Chen, G. Li, P. Jiang, *Adv. Funct. Mater.* **2013**, *23*, 506.
[32] S. Li, D. Wu, C. Cheng, J. Wang, F. Zhang, Y. Su, X. Feng, *Angew. Chem. Int. Ed.* **2013**, *52*, 12105.
[33] Y. Zhao, C. Hu, Y. Hu, H. Cheng, G. Shi, L. Qu, *Angew. Chem. Int. Ed.* **2012**, *51*, 11371.
[34] W. Yuan, J. Chen, G. Shi, *Mater. Today* **2014**, *17*, 77.
[35] W. C. Ren, H. M. Cheng, *Nat. Nanotechnol.* **2014**, *9*, 726.
[36] S. Pei, H.-M. Cheng, *Carbon* **2012**, *50*, 3210.
[37] Z. Y. Wang, Z. C. Wang, H. B. Wu, X. W. Lou, *Sci. Rep.* **2013**, *3*, 1391.
[38] P. D. Cheng, Y. H. Ni, K. F. Yuan, J. M. Hong, *Mater. Lett.* **2013**, *90*, 19.
[39] L. Fu, K. Song, X. Li, P. A. van Aken, C. Wang, J. Maier, Y. Yu, *RSC Adv.* **2014**, *4*, 36301.
[40] Y. Sun, X. Hu, W. Luo, Y. Huang, *J. Phys. Chem. C* **2012**, *116*, 20794.
[41] Z. S. Wu, W. C. Ren, L. Wen, L. B. Gao, J. P. Zhao, Z. P. Chen, G. M. Zhou, F. Li, H. M. Cheng, *ACS Nano* **2010**, *4*, 3187.
[42] G. Fang, S. Kaneko, W. Liu, B. Xia, H. Sun, R. Zhang, J. Zheng, D. Li, *Appl. Surf. Sci.* **2013**, *283*, 963.
[43] J. Zhang, J. Liang, Y. Zhu, D. Wei, L. Fan, Y. Qian, *J. Mater. Chem. A* **2014**, *2*, 2728.
[44] C. Guan, X. Li, H. Yu, L. Mao, L. H. Wong, Q. Yan, J. Wang, *Nanoscale* **2014**, *6*, 13824.
[45] F. Fan, G. Fang, R. Zhang, Y. Xu, J. Zheng, D. Li, *Appl. Surf. Sci.* **2014**, *311*, 484.
[46] C. Guan, X. L. Li, H. Yu, L. Mao, L. H. Wong, Q. Y. Yan, J. Wang, *Nanoscale* **2014**, *6*, 13824.
[47] S. J. R. Prabakar, Y.-H. Hwang, E.-G. Bae, S. Shim, D. Kim, M. S. Lah, K.-S. Sohn, M. Pyo, *Adv. Mater.* **2013**, *25*, 3307.
[48] Z. Y. Wang, Z. C. Wang, W. T. Liu, W. Xiao, X. W. Lou, *Energy Environ. Sci.* **2013**, *6*, 87.
[49] S. Yang, W. Yue, J. Zhu, Y. Ren, X. Yang, *Adv. Funct. Mater.* **2013**, *23*, 3570.
[50] H. K. Wang, A. L. Rogach, *Chem. Mater.* **2014**, *26*, 123.